Stretchable high-entropy alloy nanoflowers enable enhanced alkaline hydrogen evolution catalysis

Min Wei [a], Yuyan Sun [a], Fei Ai [a], Shibo Xi [b], Junyu Zhang [a], Jike Wang [a],*

[a] *The Institute for Advanced Studies, Wuhan University, Wuhan 430072, China*
[b] *Institute of Chemical and Engineering sciences, A*STAR (Agency for Science, Technology and Research) Singapore 627833, Singapore*

ARTICLE INFO

ABSTRACT

High-entropy alloys have received much attention in many fields for their unique physicochemical properties, yet precise control at the atomic level in terms of size and morphology remains a great challenge. Herein, we report a kind of stretchable Pt(Co/Ni)MoPdRh HEAs nanoflowers (NFs) assembled by ultra-thin nanosheets ($\sim$ 1.68 nm) for alkaline hydrogen evolution reaction (HER) via one-step wet chemical strategy. The mass activity of HEA NFs reaches 16.64 A mg_{HEA}^{-1}, which is 6.38 times higher than that of commercial Pt/C. The enhanced HER performance and stability is attributed to the multiple active sites in HEAs for reducing the water dissociation energies barriers as well as favoring H adsorption and the strain effect induced by unique structure. This work not only provides a general method for synthesizing unique structures of high entropy alloys, but also provides a fundamental understanding for the study of catalysis in HEAs.

1. Introduction

Hydrogen fuel is considered as one of the cleanest and most promising energy sources due to its free pollution and highly efficient energy density, which is expected to be an alternative to fossil fuels [1–3]. And green hydrogen from electrocatalytic water splitting is regarded as the friendliest and promising technology for achieving efficient utilization of renewable energy storage and carbon neutrality [4–6]. Over the past decades, much efforts have been focused on exploring highly active catalysts for hydrogen evolution reaction (HER) to improve the energy conversion efficiency of water electrolysis with proton exchange membranes [7,8]. The desired high-activity catalysts are generally characterized by high-level activity, favorable stability and high active-site utilization. Up to now, Pt-based catalysts are still the representative catalysts for high activity HER and have been widely used in recent decades due to their effective catalytic activity [9,10]. Energy scarcity, high cost and poor stability of Pt restrict its wider application. Therefore, improving the intrinsic activity and exposing more active sites of Pt to achieve higher catalytic performance are crucial for the study of Pt-based catalysts.

In recent years, high-entropy alloys and even high-entropy oxide have been drawn increasing attention in various fields such as superconductivity, heterogeneous catalysis and power battery on account of

their high thermal stability, strong mechanical strength, excellent corrosion resistance and good performance [11–13]. Similarly, the cocktail effect due to the high structural dependence of the high-entropy alloy has a significant enhancement on the activity as well as the stability of the heterogeneous electrocatalysis [14–16]. Therefore, it is critical to moderate the HEA structure to achieve high performance in the field of catalysis. There are generally two main aspects to optimize the catalyst. On one hand, the size of the catalyst produces electronic and geometric effects. The smaller the size of the surface atoms, the lower the coordination number of metal atoms, and thus exposing more unsaturated metal atoms, i.e., active sites, and significantly increasing the specific activity of the catalyst. For example, $Pt_{18}Ni_{26}Fe_{15}Co_{14}Cu_{27}$ nanoparticles (NPs) with a size of $\sim$3.4 nm exhibit enhanced electrocatalysis towards methanol oxidation reaction (MOR) due to the multi-active sites on the HEA surface and ultra-small NPs size, which would promote the proton and intermediate transformation [17]. Wang et al. demonstrated that Fe surrounded by alloy metals in RuFeCoNiCu NPs with $\sim$16 nm is the best site for N_2 adsorption and activation, Co-Cu and Ni-Ru couples show an excellent capacity to surface hydrogenation at low overpotential [18]. Furthermore, Sub-2 nm ultrasmall PtRhFe-CoNi NPs have been reported and applied in efficient acidic electrolyte HER [19].

On the other hand, regulating the electronic structure by tailored

---

morphologies is another proven approach. Among the catalyst structures in different dimensions, ultra-thin two-dimensional (2D) structures with large specific surface area, abundant active sites and high density of unsaturated atoms have proven to be ideal structures for engineering advanced catalysts in their surface-related applications [20,21]. However, achieving two-dimensional anisotropic growth of multicomponent nanocrystals remains a great challenge due to the different nucleation/growth kinetics of different component metals in HEAs [22].

Herein, we develop a one-step wet chemical strategy to synthesize a PtCoMoPdRh/ PtNiMoPdRh HEAs NFs assembled by the ultra-thin nanosheets. The obtained PtCoMoPdRh NFs exhibit an enhanced electrochemical activity and stability towards alkaline HER. The mass activity of PtCoMoPdRh NFs reaches 16.64 A mg_{HEA}^{-1}, which is 6.38 times higher than that of commercial Pt/C (2.61 A mg_{Pt}^{-1}). The formation mechanism of nanoflowers and the role of the constituent elements in regulating the electronic structure are also discussed. The enhanced HER performance is attributed to the multiple active sites in HEAs and the strain effect induced by unique structure. Combined with DFT theoretical calculation it was found that the reduced water dissociation energy barriers and the facilitation of H adsorption are mainly attributed to the multiple active sites in HEA, and the appropriate strain is favorable for H adsorption, thus enhancing both the Volmer step and Tafel step in the alkaline HER. And among these constituent metal elements of the HEA,

Pt is the main active sites for H adsorption, while Co and Mo are favorable for water adsorption and thus activate the water dissociation. This work may not only provide a facile strategy for controllable synthesis of PtCoMoPdRh/PtNiMoPdRh HEA NFs, but also lays the foundation for an understanding of the catalytic mechanisms of high-entropy alloys in aspect of strain effect and multi-active sites for multi-steps in alkaline HER.

2. Results and discussions

The novel HEA NFs was synthesized by one-step wet chemical strategy (Fig. 1a). Firstly, an equimolar proportion of acetylacetonate metal salts (Pt, Co/Ni, Mo, Pd, Rh) were dissolved in triethyleneglycol (TEG) under surfactant triethyl benzyl ammonium chloride (TEBA), and after a few hours of homogeneous stirring, D-(+)-Glucose-TEG solution and molybdenum hexacarbonyl ($Mo(CO)_6$) were added to the above solution. The NFs was synthesized by the reduction of glucose and modification of TEBA.

As shown in Fig. 1b, c, the representative high-angle annular dark-field scanning transmission electron microscope (HAADF-STEM) at low magnification images of PtCoMoPdRh NFs indicates that the PtCoMoPdRh HEA is a flower-like structure, which is assembled by ultra-thin nanosheets. The thickness of the nanosheet obtained by atomic force
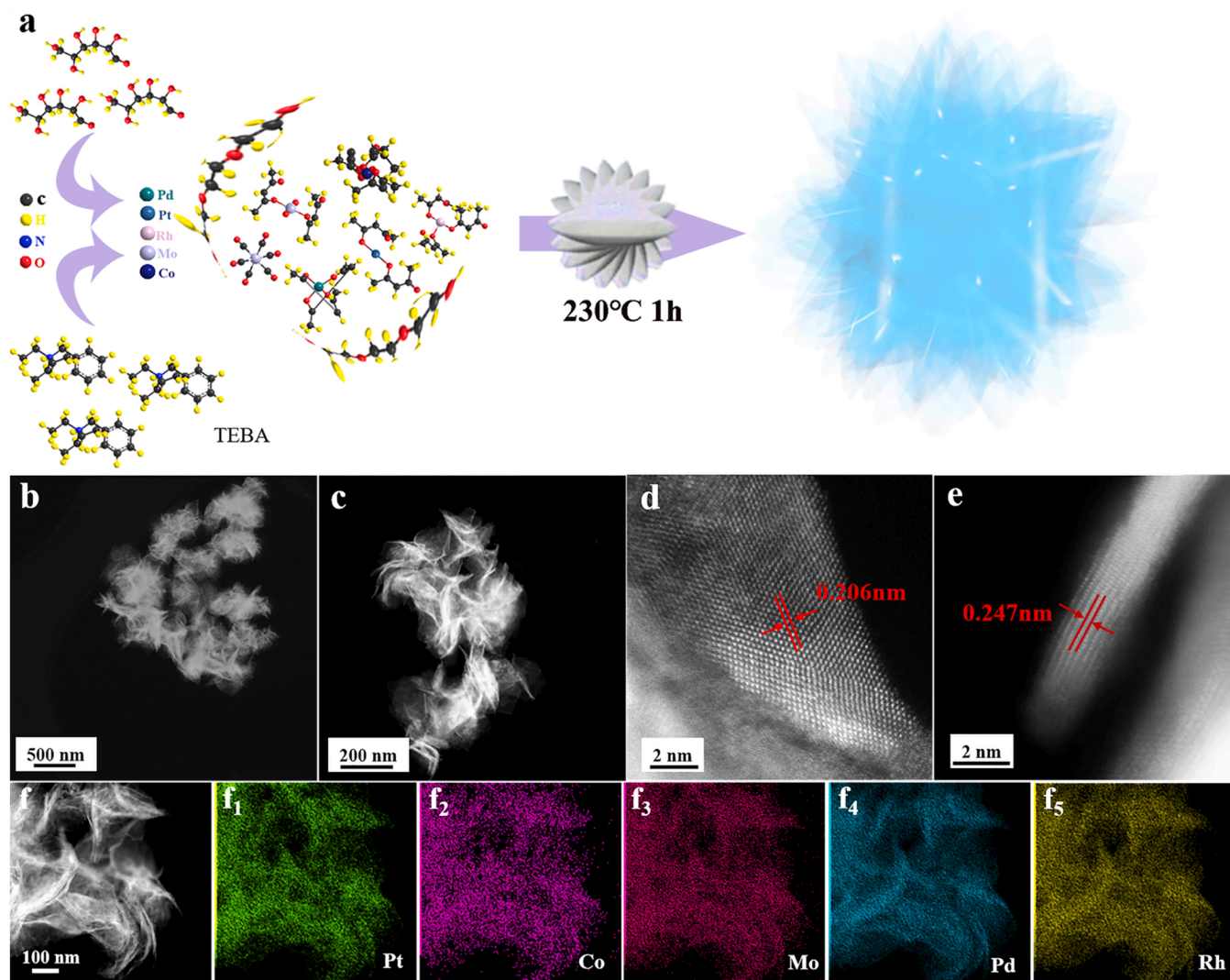

Fig. 1. (a) The synthesis scheme of PtCoMoPdRh/PtNiMoPdRh NFs. (b) (c) HAADF-STEM images, (d) (e) HR-STEM images of different areas of the nanosheets of PtCoMoPdRh NFs. (f) HAADF-STEM image and (f_{1-5}) the corresponding EDS mapping of PtCoMoPdRh NFs.

microscope (AFM) characterization is 1.68 nm (Fig. S1). To investigate the atomic structure of PtCoMoPdRh NFs, High-resolution scanning transmission election microscope (HR-STEM) images at two different areas were exhibited in Fig. 1d, e. The fringe pattern of nanosheets and the position which petals curling up display lattice spacing of 0.206 nm and 0.247 nm, which are corresponding to the 9.6 % compressive strain and 8.3 % stretch compared to 0.228 nm of standard metallic Pt (1 1 1) [23]. The compressive and stretch effects of the lattice are mainly a consequence of the formation of high entropy alloys and the unique morphology. Furthermore, Energy Dispersive Spectrometer (EDS) mapping of PtCoMoPdRh NFs (Fig. 1f, f_{1-5}) obviously show that Pt, Co, Mo, Pd, Rh are evenly distributed throughout the NFs, demonstrating that the NFs is composed of Pt, Co, Mo, Pd and Rh. And inductively coupled plasma atomic emission spectrometry (ICP-AES) result shows that the atomic ratio of Pt/Co/Mo/Pd/Rh in PtCoMoPdRh NFs is 35/7/8/23/27 (Fig. S2), which is close to the EDS result shown in Fig. S3. This means the moral ratio of Pt/Co/Mo/Pd/Rh in PtCoMoPdRh NFs is also 35/7/8/23/27, which is a kind of high entropy alloy [24]. In addition, the HR-STEM image and corresponding EDS mapping show that the Pt, Co, Mo, Pd and Rh are distributed uniformly (Fig. S4). And the atomic ratio of Pt/Co/Mo/Pd/Rh is 33/9.3/5.3/32.8/19.5, which is close to the low spatial resolution EDS result, demonstrating that the constituent elements mix at atomic level.

Meanwhile, PtNiMoPdRh NFs was synthesized by the same one-step liquid-phase synthesis strategy. As shown in Fig. S5, Pt, Ni, Mo, Pd, Rh are uniformly dispersed in the whole nanoflower structure, and the atomic ratio of Pt/Ni/Mo/Pd/Rh in PtNiMoPdRh NFs is 10.5/9.5/7.6/37.1/35.2. It is further demonstrated that this method is universal and is expected to be used for the synthesis of nanoflower structures of other components to regulate the electronic configuration of HEAs and thus achieve a higher catalytic activity.

Besides, the morphology and structure information of PtCoMoPdRh NPs are shown in Fig. S6. It's clear shown that the size of PtCoMoPdRh NPs is about 2.0–2.4 nm. And the element content analysis at low resolution were conducted by EDS-mapping, Pt, Co, Mo, Pd and Rh are distributed uniformly throughout the structure of the nanoparticles. And the atomic ratio of Pt/Co/Mo/Pd/Rh is 26.9/6.3/7.8/34.4/24.6.

In addition, the role of constituent metals in the formation of PtCoMoPdRh NFs were investigated by the quaternary alloy of PtCoMoRh, PtCoPdRh, PtCoMoPd, PtMoPdRh and CoMoPdRh. Firstly, the precursors of Pt, Co, Mo and Rh were reaction in the same synthesis condition of PtCoMoPdRh NF, but no product was obtained. Meanwhile, PtCoPdRh, PtCoMoPd, PtMoPdRh and CoMoPdRh quaternary alloys were obtained under the same reaction conditions. This result show that Pd plays key role in the formation of PtCoMoPdRh alloy. And for the role of Mo in the process of HEAs nanoflowers, the morphology of PtCoPdRh, PtCoMoPd, PtMoPdRh and CoMoPdRh quaternary alloys were investigated. As shown in Fig. S7-9, it's obviously show that the quaternary alloys of PtCoMoPd, PtMoPdRh and CoMoPdRh are nanoflowers structure. And the morphology of PtCoRhPd quaternary alloy is a kind of nanoparticles (Fig. S10). This comparison confirmed that Mo is the essential for the formation of nanoflower structure. Besides, since the different redox potentials of the constitute metals, galvanic replacement occurs during the reduction process in liquid phase synthesis, which ultimately affects the atomic ratio of the alloy component. In addition, the role of constitute metals in regulating electronic environment are different, which would affect the atomic ratio in HEAs. As shown in Fig. S7-9, the atomic ratio of Pt/Co/Mo/Pd, Pt/Mo/Pd/Rh and Co/Mo/Pd/Rh of PtCoMoPd NFs, PtCoPdRh NFs and CoMoPdRh NFs are 8.2/12.6/6.3/72.9, 19.2/7.0/68.1/5.7 and 7.1/5.3/79.2/8.4, respectively.

The diffraction peaks of PtCoMoPdRh nanoparticles (NPs), PtCoMoPdRh NFs are located at 40.12°, 46.58°and 68.11° in X-ray diffraction (XRD) patterns (Fig. S11), which are assigned to the (1 1 1), (2 0 0), and (2 2 0) facets of the face-centered-cubic (fcc) crystal structure, respectively. Comparing to commercial Pt/C and standard Pt (PDF#70–2431), PtCoMoPdRh NPs (located at 40.15°) have a positive

shift of about 0.41°, which means that the interatomic distances between adjacent Pt sites is decreased by the formation of HEAs. Meanwhile, the PtCoMoPdRh NFs (located at 40.05°) occurs 0.1° negative shift with respect to PtCoMoPdRh NPs, indicating lattice compression and stretching occurred in HEA NFs compared to PtCoMoPdRh NPs induced by the formation of unique morphology. To further investigate the strain in HEAs, the lattice parameters was estimated from the position of the (1 1 1), (2 0 0) and (2 2 2) diffraction peaks on commercial Pt/C, PtCoMoPdRh NPs and PtCoMoPdRh NFs. As shown in Table S1, comparing to commercial Pt/C, the lattice constants in Pt of PtCoMoPdRh NPs and PtCoMoPdRh NFs have 1.47 % and 1.34 % contraction due to the alloying in HEA. PtCoMoPdRh NFs show 0.13 % stretch in comparison with PtCoMoPdRh NPs, which induced by the unique morphology. The strain induced by alloying and morphological structure in HEAs favors the modulation of d-electron occupancy state, which in consequence affects the electrochemical catalytic activity [25].

Besides, XPS measurement was characterized to further investigate the surface electronic structure of PtCoMoPdRh NFs and PtCoMoPdRh NPs. As shown in Fig. 2a, the PtCoMoPdRh NFs Pt 4f spectra show two intense peaks at 71.08 and 74.43 eV are metallic Pt from Pt $4f_{7/2}$ and Pt $4f_{5/2}$, respectively. And the two more fitted peaks at 71.86 and 75.24 eV are assigned to oxidized Pt, which may originate from oxygen adsorption on Pt. As shown in Fig. S13a, the Pt $4f_{7/2}$ of PtCoMoPdRh NPs (71.17 eV) and PtCoMoPdRh NFs (71.07 eV) exhibit a negative shift compared to commercial Pt/C (74.15 eV), demonstrating that the electron migration induced by alloying in HEA. As shown in Fig. 2b, the two fitting peaks located at about 780.69 and 796.73 eV, accompanied by two prominent shake-up satellite peaks (~785.70 and ~802.19 eV) can be assigned to Co^{2+} $2p_{3/2}$ and $2p_{1/2}$, respectively [26]. Fig. 2c display three fitting peaks at 227.89, 230.98 and 232.10 eV are ascribed to Mo^0, Mo^{4+} and Mo^{6+} $3d_{5/2}$, respectively. And the peaks at approximately 228.46, 234.04 and 235.33 eV are corresponding to Mo^0, Mo^{4+} and Mo^{6+} $3d_{3/2}$ [27]. The Pd 3d spectrum in Fig. 2d show that the two intense peaks located at ~335.13 and ~ 340.38 eV are associated with metallic Pd. And another two concentrated peaks at about 336.11 and 341.23 eV are assign to the oxidated Pd [28]. Moreover, a spin-orbit doublet at 306.9 eV (Rh $3d_{5/2}$) and 311.7 eV (Rh $3d_{3/2}$) binding energies shown in Fig. 2e are associated with the metallic Rh, while peaks located at 307.8 eV (Rh $3d_{5/2}$) and 312.3 eV (Rh $3d_{3/2}$) are indicative of the presence of oxidated Rh [29]. In consideration of the overlay of Rh $3d_{3/2}$ and Pt $4d_{5/2}$ orbitals, the additional peaks centered at 314.4 eV near Rh 3d spectrum are assigned to the Pt $4d_{5/2}$ [30]. In addition, the O 1s spectrum of PtCoMoPdRh NFs (Fig. 2f) reveals peak at 531.8 eV, which is ascribed to surface adsorbed oxygen/hydroxyl groups (O_2/OH^-). There are no peaks exhibited for lattice O^{2-} of metal oxides [31]. These results show the presence of Pt-Co-Mo-Pd-Rh based surface (oxy) hydroxides, which is natural due to their high surface-to-volume ratio.

Furthermore, a comparison of NPs and NFs XPS spectrums is used to illustrate the effect of morphology on the surface electronic structure. The full survey scan spectra of PtCoMoPdRh NPs and PtCoMoPdRh NFs shown in Fig. S12 disclose that Pt, Co, Mo, Pd and Rh are contained in HEAs. Remarkable, the Pt $4f_{7/2}$ of PtCoMoPdRh NFs has 0.1 eV negative shifted (Fig. S13a), which is attributed to the formation of NFs and thus enhanced the interaction of component metals. And the binding energy of Co $2p_{3/2}$, Mo^0 $3d_{5/2}$, Pd^0 $3d_{5/2}$ and Rh^0 $3d_{5/2}$ in PtCoMoPdRh NFs have a negative shift of 1.01, 0.21, 0.12, and 0.17 eV in comparison with PtCoMoPdRh NPs (Fig. S13b-e), demonstrating that the electronic structure of constituent elements in HEA varies induced by the morphology. And the O 1s spectra of PtCoMoPdRh NPs and PtCoMoPdRh NFs (Fig. S13f) show that the oxidation state of the constitute metals surface is derived from the surface adsorbed oxygen/hydroxyl groups.

In aspect of the regulation of constitute metals for electronic environment in PtCoMoPdRh NFs, the XPS of PtCoPdRh NPs and quaternary alloy nanoflowers (PtCoMoPd NFs, CoMoPdRh NFs and PtCoPdRh NFs)
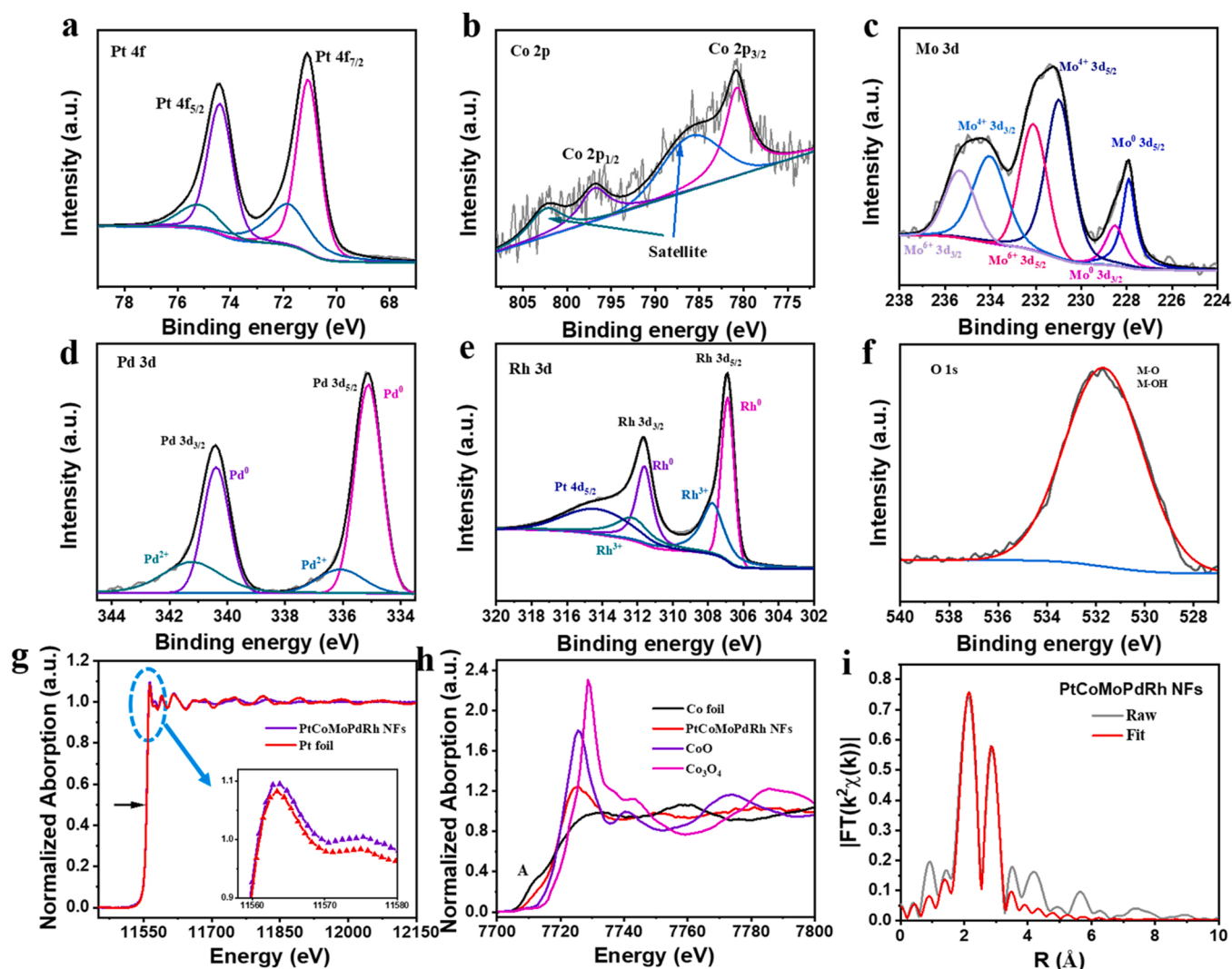
Fig. 2. XPS spectra of (a) Pt 4f, (b) Co 2p, (c) Mo 3d, (d) Pd 3d, (e) Rh 3d and (f) O 1s of PtCoMoPdRh NFs. Normalized X-ray absorption near-edge structure (XANES) at the (g) Pt L_3-edge; inset: corresponding white line (WL) of PtCoMoPdRh NFs and Pt foil. (h) Normalized XANES Co K-edge of Co foil, PtCoMoPdRh NFs, CoO and Co_3O_4. (i) Fourier-transformed magnitude of Pt L_3-edge extended X-ray absorption fine structure (EXAFS) in the R space and the corresponding fitting curves of PtCoMoPdRh NFs.

were compared with the obtained PtCoMoPdRh NPs and PtCoMoPdRh NFs. The XPS spectra and the fitting curve of Pt 4f, Co 2p, Mo 3d, Pd 3d and Rh 3d are shown in Fig. S14a-e. In order to accurately compare the binding energy change of the constitute metals in different structure, the binding energy of Pt $4f_{7/2}$, Co $2p_{3/2}$, Mo^0 3d, Pd $3d_{5/2}$ and Rh $3d_{5/2}$ of PtCoPdRh NPs, PtCoMoPdRh NPs, PtMoPdRh NFs, PtCoMoPd NFs, CoMoPdRh NFs and PtCoMoPdRh NFs are listed in Table S2. For the comparison of PtCoPdRh NPs and PtCoMoPdRh NPs, the introduction of Mo causes the binding energy of Pt $4f_{7/2}$, Pd $3d_{5/2}$, Rh $3d_{5/2}$ to be negative shift, while the binding energy of Co $2p_{3/2}$ is positively shift in PtCoMoPdRh NPs (Fig. S14f). The introduction of Mo modulates the electronic structure in PtCoMoPdRh HEAs and promotes the degree of electron gain and loss of Co. Among the binding energies change of constitute metals, the change of Pd is the most significant, with an offset of 0.24 eV, indicating that the electronic structure of Pd changes significantly in the PtCoMoPdRh HEAs. Meanwhile, For the comparison of the PtMoPdRh NFs and PtCoMoPdRh NFs (Fig. S14g), the introduction of Co shifts the binding energy of other constitute metals negatively, where Pt $4f_{7/2}$, Mo^0, Pd $3d_{5/2}$ and Rh $3d_{5/2}$ shift by 0.12, 0.38, 0.35 and 0.31 eV, respectively. This result indicates that the main role of Co in the PtCoMoPdRh NFs structure is to lose electrons and regulate the electronic structure of other metals. And by comparing PtCoMoPd NFs,

CoMoPdRh NFs and PtCoMoPdRh NFs (Fig. S14g), the introduction of Rh and Pt makes a positive shift in the binding energy of Co, indicating that Rh and Pt are involved in electron gain and loss in the PtCoMoPdRh NFs and interact directly with Co. These comparisons verifies that the constitute metals play an important role in regulating the electronic environment, where the change of Co, Mo, Pd and Rh are significant.

Synchrotron X-ray absorption near-edge structure (XANES) and extended X-ray absorption fine structure (EXAFS) of Pt foil, Co foil and PtCoMoPdRh NFs are analyzed for the atomic arrangement and chemical coordination environment. As shown by the black arrow in Fig. 2g, the position of the inflection point in XANES refers to the threshold energy for 2p to 5d electron transition, and is generally proportional to the oxidation state of Pt. Obviously, positions of the inflection point of PtCoMoPdRh NFs is identical to that of Pt foil, which illustrates the metallic characteristic of Pt in PtCoMoPdRh NFs [32]. The white line (WL) intensity of Pt L_3-edge XANES signal is in direct correlation with the density unoccupied Pt 5d orbitals [33]. As shown in the insect image of Fig. 2g, the WL intensity of PtCoMoPdRh NFs is stronger than that of Pt foil, implying that the Pt 5d electronic orbitals have changed in the PtCoMoPdRh NFs compared to Pt foil and possess higher occupied states in Pt 5d orbital. Meanwhile, Fig. 2h displays the XANES spectra of Co K-edge for Co foil and PtCoMoPdRh NFs. The intensity of the pre-edge

band (peak A) of PtCoMoPdRh NFs decreases while the WL intensity increases compared to Co foil. This change is attributed to electron transfer from Co to other constituent metals in PtCoMoPdRh NFs and rearrangements between the 3d, 4s and 4p layers of Co, indicating strong interactions between the constituent metal atoms [34].

To further clarify the coordination of PtCoMoPdRh NFs, the Fourier transform (FT) and wavelet transform (WT) of Pt L$_3$-edge EXAFS spectra was analyzed. The FT-EXAFS spectrum of Pt L$_3$-edge and the corresponding fitting result display that the peak in R space of Pt foil is 2.76 Å (Fig. S15 and Table S3), which is attributed to the contribution of the first Pt-Pt coordination shell. Meanwhile, as shown in Fig. 2i, the first coordination shell in Pt L$_3$-edge of PtCoMoPdRh NFs is composed by the Pt-Rh, Pt-Pt and Pt-Co scattering paths, and the corresponding bond length (R$_{Pt-M}$) are 2.72, 2.70 and 2.73 Å, respectively. Wavelet transform (WT) EXAFS analysis (Fig. S15d,h) reveals that the Pt-M paths slightly shift to a lower k space in PtCoMoPdRh NFs in contrast to Pt foil. The decrease of Pt-Pt bond length and the change of Pt coordinate environment probably result from the strain effect induced by the alloying and morphology regulation in PtCoMoPdRh NFs, which would contribute to the boost electrocatalytic performance.

In addition, to further study the coordination environment of Co, the extended edges of the Co K-edge were fitted based on the HEA model and the corresponding results are shown in Fig. S16 and Table S4. Apparently, the first coordination shell in Co K-edge of PtCoMoPdRh NFs is composed by the Co-Pt, Co-Co, Co-Pd and Co-Rh scattering paths, and the corresponding bond length (R$_{Pt-M}$) are 2.73, 2.51, 2.77 and 2.76 Å, respectively. This result indicates that Co coordinates with other metallic elements and forms alloy phases in PtCoMoPdRh NFs. Furthermore, as shown in Fig. S17, the WT-EXAFS of Co foil clearly show that Co-Co bond is located at ∼ (9.9 Å^{-1}, 2.2 Å), the Co-O bond of CoO and Co$_3$O$_4$ is located at (13.6 Å^{-1}, 1.4 Å), thus the scatter path of PtCoMoPdRh NFs located at (9.7 Å^{-1}, 2.2 Å) is assigned to Co-M bond. This result further confirmed that the metallic state of Co in PtCoMoPdRh HEAs.

2.1. Electrochemical activity

Alkaline water electrolysis shows clear advantages (such as long-term stability, mature commercialization) versus acidic water electrolysis for large-scale and low-cost hydrogen production. Thus, the HER performance of commercial Pt/C, PtCoMoPdRh NPs and PtCoMoPdRh NFs were evaluated in 1.0 M KOH electrolyte. In order to accurately evaluate the electrochemically active area of catalysts, the double layer capacitance (C$_{dl}$) method was conducted in this work [35,36]. The C$_{dl}$ of PtCoMoPdRh NFs (0.0512 mF) shown in Fig. 3a and Fig. S18 is higher than that of PtCoMoPdRh NPs (0.0028 mF) and commercial Pt/C (0.00102 mF), indicating that PtCoMoPdRh NFs has largest electrochemical active surface area (ECSA) with enriched active sites and thus enhanced the activity in alkaline electrolyte. Comparing to PtCoMoPdRh NPs, PtCoMoPdRh NFs show larger ECSA, indicating that the unique structure would expose more active sites for HER. The overpotential at a current density of −10 mA cm^{-2} (corresponding to an efficiency of about 12% for a solar-hydrogen device) is a key benchmark for evaluating the activity of HER [37,38]. It's obviously exhibit that both PtCoMoPdRh NFs and PtCoMoPdRh NPs present enhanced HER activity with respect to commercial Pt/C. The overpotential of PtCoMoPdRh NFs (16.5 mV) at current density of −10 mA cm^{-2} is lower than that of PtCoMoPdRh NPs (36.1 mV), and even better than 62.4 mV of commercial Pt/C (Fig. 3b). The overpotential difference in PtCoMoPdRh NPs and NFs demonstrates that the reaction energy barrier of PtCoMoPdRh NFs is much lower than that of NPs, and thus enhanced HER performance. Meanwhile, the intrinsic activity of the catalyst could be clearly obtained from the current density plot with normalized the active metals amount. Considering that other transition metals would contribute to the HER performance under alkaline conditions, the current density normalized by the all-metal amount has calculated. As
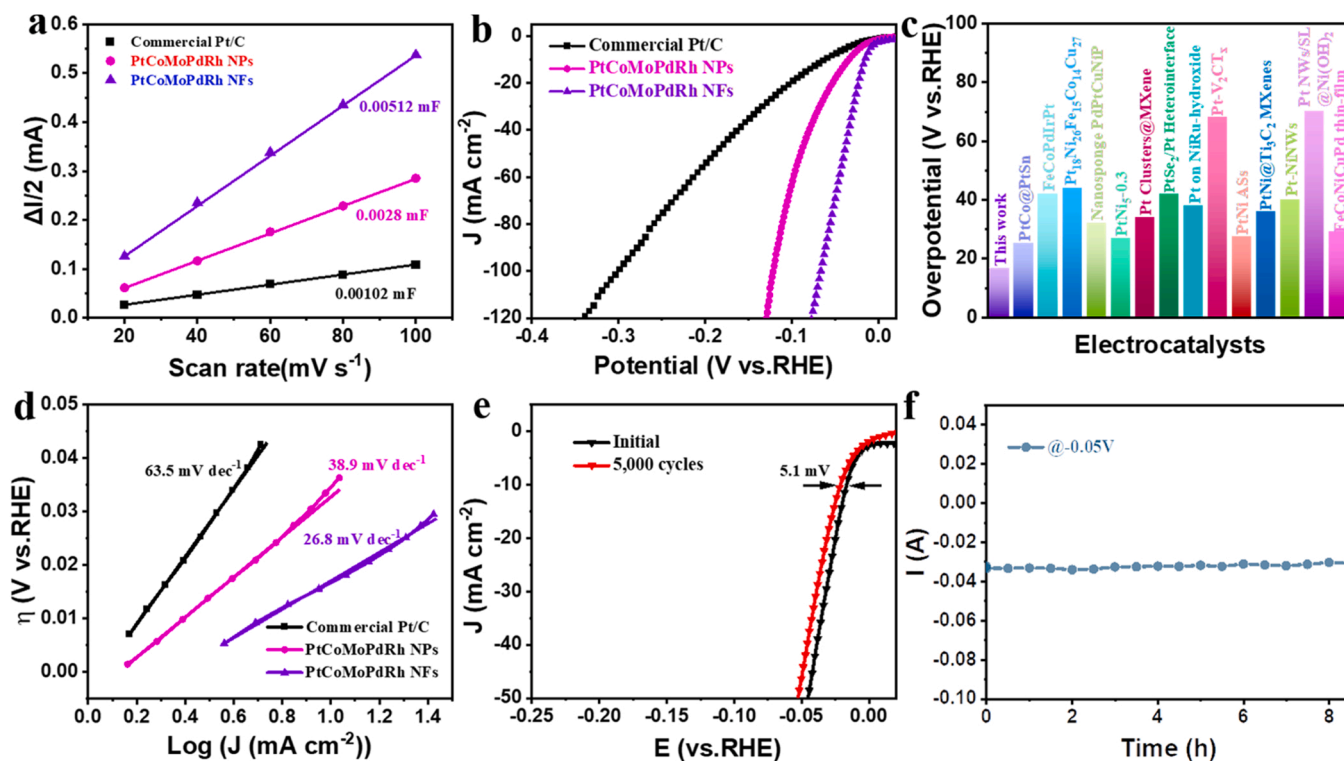

Fig. 3. (a) the double-layer capacitance, (b) LSV curves of PtCoMoPdRh NFs, PtCoMoPdRh NPs and commercial Pt/C. (c) Comparison of the overpotentials of PtCoMoPdRh NFs and most of reported Pt-based catalysts at a current density of −10 mA cm^{-2}. (d) the Tafel slope curve obtained by LSV of PtCoMoPdRh NFs, PtCoMoPdRh NPs and commercial Pt/C. (e) LSV curves before and after accelerated durability tests (ADTs) for 5000 cycles, (f) chronoamperometry (CA) curve at −0.05 V vs. RHE of PtCoMoPdRh NFs.

shown in Fig. S19a, at a current density of -10 mA cm^{-2} with the same loading amount, the PtCoMoPdRh NFs require the lowest overpotential, which implies that the superior activity of PtCoMoPdRh NFs. In addition, the mass activity was calculated based on the overpotential $(-62.4 \text{ mV vs. RHE})$ at the current density of -10 mA cm^{-2} of commercial Pt/C with normalized by constituent metals loading. As shown in Fig. S19b, the mass activity of PtCoMoPdRh NFs ($16.64 \text{ A mg}_{HEA}^{-1}$) is 3.49 and 6.38 times of PtCoMoPdRh NPs ($4.76 \text{ A mg}_{HEA}^{-1}$) and commercial Pt/C ($2.61 \text{ A mg}_{Pt}^{-1}$) respectively, suggesting that the PtCoMoPdRh NFs require the lower energy consumption to achieve the same production of H_2.

Comparing to previous reported Pt-based catalysts shown in Fig. 3c, the overpotential at current density of -10 mA cm^{-2} is much lower than that of most Pt-based catalysts, implying its outstanding electrocatalytic activity. And the electrochemical impedance spectroscopy (EIS) constructed at -0.01 V vs. RHE, as shown in Fig. S20, further verify that PtCoMoPdRh NFs display excellent interfacial charge transfer kinetics and enhanced HER activity due to the lower charge-transfer resistance (Rct), comparing to the commercial Pt/C and PtCoMoPdRh NPs. Besides, the Tafel slope indicates the intrinsic nature of the catalyst and is utilized to analyze the rate determining step of HER. As shown in Fig. 3d, the Tafel slope of PtCoMoPdRh NFs (26.8 mV dec^{-1}) is lower than that of commercial Pt/C (63.5 mV dec^{-1}) and PtCoMoPdRh NPs (38.9 mV dec^{-1}), suggesting that the Volmer-Tafel mechanism (30 mV dec^{-1}) domains in the HER progression of PtCoMoPdRh NFs [39]. Furthermore, the exchange current density (j_0) derived from the Tafel plot is another important kinetic parameter for HER. As shown in Fig. S21, the j_0 of PtCoMoPdRh NPs is higher than commercial Pt/C, demonstrating that the redox electron pair of PtCoMoPdRh NPs has faster reaction kinetic with higher intrinsic catalytic activity due to the alloy effect [40]. Besides, the PtCoMoPdRh NFs show higher j_0 comparing to PtCoMoPdRh NPs, further verify the enhanced intrinsic activity due to this kind of unique structure.

HER stability of PtCoMoPdRh NFs was evaluated by ADTs for 5000 cycles and chronoamperometry (CA), respectively. As shown in Fig. 3e, the HER activity loss of PtCoMoPdRh NFs is almost neglectable, and the overpotential is only have a negative shift of 5.1 mV, compared to its initial value. Meanwhile, the overpotential loss of commercial Pt/C is 17.5 mV (Fig. S22), which is much larger than PtCoMoPdRh NFs. And the STEM-EDS images (shown in Fig. S23) of PtCoMoPdRh NFs after ADTs display that the nanostructure and morphology is still remains, implying that the enhanced stability of PtCoMoPdRh NFs. In addition, the CA curve shown in Fig. 3f exhibits that the current almost unchanged after more than 8 h under continuous voltage. Further illustrating the excellent stability of PtCoMoPdRh NFs. The high catalytic activity of PtCoMoPdRh NFs is mainly attributed to the efficient electron transport, multi-active sites and the lattice distortion. And the strain effect of atomic contraction also has great effect on the structure stability and thus enhanced the electrochemical durability.

2.2. DFT calculation

DFT theoretical calculations are implemented to further comprehensive understand the catalytic mechanism of PtCoMoPdRh HEAs. The calculated model in the top view and side view of $Pt_{35}Co_5Mo_{10}Pd_{25}Rh_{25}$ (1 1 1) presents in Fig. S24, and the corresponding total density of states (TDOS) (Fig. S25) are larger than 0 at Femi level (E_F), implying the metallic nature of the HEA [41]. To identify the role of individual metal sites and the multi-active sites in HEAs, the H and H_2O absorption on the top site were iterated over respectively. In the alkaline HER electrolysis, the first step in the reaction occurs is the dissociation of water. As shown in Table S5, the adsorption energy of water varies at different sites which is attributed to the different surrounding electronic environment. By comparing the initial position of water molecule adsorption and the position after optimization, the water molecule is more stable at the top sites and all five constituent components contribute to the water

adsorption in the process of alkaline HER. In general, the activity of any catalytic reaction is related to the d-band center of the metal under consideration. Therefore, d-band centers of all of the Pt atoms present on the topmost layer of the $Pt_{35}Co_5Mo_{10}Pd_{25}Rh_{25}$ (1 1 1) HEA slab have been plotted in Fig. S26. Among the top active sites of $Pt_{35}Co_5Mo_{10}Pd_{25}Rh_{25}$ (1 1 1), the Pt16 atoms with (0.106, 0.340, 0.482) vs. fractional coordinate compared to the origin (0 0 0) has the closest to Fermi level. Hence, it was chosen as one of the catalytic centers for both water dissociation and hydrogen adsorption [42]. Firstly, the water dissociation energy barrier was considered, since the whole alkaline HER kinetics is regulated by the Volmer step ($M + H_2O + e^- = M–H^* + OH^-$). As shown in Fig. 4a-c, the activation energy of water dissociation on Pt16 in $Pt_{35}Co_5Mo_{10}Pd_{25}Rh_{25}$ (1 1 1) are significantly decrease from 0.57 to 0.16 eV compared to pure Pt (1 1 1), implying that the chemical environment change the electronic structure and thus vastly accelerating the sluggish Volmer step [43,44].

Moreover, the adsorption free energy of hydrogen (ΔG_{H^*}) is another crucial criterion to evaluate Tafel step ($2 M–H^* = 2 M + H_2$) of alkaline HER performance. Catalysts with hydrogen adsorption free energy less than and close to zero ($\Delta G_{H^*} \approx 0$) are considered to be optimum [45]. In this regard, the hydrogen absorption on top active sites of $Pt_{35}Co_5Mo_{10}Pd_{25}Rh_{25}$ (1 1 1) were also calculated to verify the multi active sites in HEAs (Table S6). Impressively, the results show that ΔG_{H^*} for most of the active sites was greater than that of Pt (1 1 1) (-0.30 eV) at the top active sites, reflecting the existence of multiple active sites in HEA. ΔG_{H^*} of some representative active sites plotted in Fig. 4d, the H adsorption after optimization on top$_{Pt}$ sites to form M-H* and ΔG_{H^*} are lower than that of Pt (1 1 1), demonstrating that Pt top sites in $Pt_{35}Co_5Mo_{10}Pd_{25}Rh_{25}$ (1 1 1) behave as the main and direct active site in the Tafel step. Meanwhile, when hydrogen is adsorbed on the top sites of Rh, Pd, Mo, and Co, almost M-H* on top sites are not formed, and instead falls on hexagonal close-packed (hcp) sites. It is suggested that Rh, Pd, Mo and Co sites regulates the local chemical environment and thus improving the HER activity of HEAs [41].

To further investigate the strain effect in HEAs, the effect of strain from -3 – 3 % on Tafel step is explored on the $Pt_{35}Co_5Mo_{10}Pd_{25}Rh_{25}$ (1 1 1). As shown in Fig. 4e, f, the ΔG_{H^*} on Pt16 is close to zero with the compressive increase from 0 % to 3 % and the Tafel step accelerates as the stretching increasing, which demonstrating that strain can effectively modify the electronic properties of HEAs and thus enhance the HER performance [46].

3. Conclusion

In this work, novel PtCoMoPdRh/PtNiMoPdRh NFs assembled by radial ultra-thin nanosheets, with the approximately 1.68 nm thickness, were successfully synthesized by one-step wet chemical strategy. The strain effect and cocktail effect of PtCoMoPdRh NFs are induced unique morphology and structural disorder. PtCoMoPdRh NFs exhibit enhanced alkaline HER activity and durability, in which the mass activity ($16.64 \text{ A mg}_{HEA}^{-1}$) is 6.38-fold higher than that of commercial Pt/C and both morphology and content remains unchanged after stability test. Pd and Mo plays key role in the formation of alloys and nanoflowers in both quaternary and quintuplet alloys of Pt(Co/Ni)MoPdRh system. And the role of Rh, Mo, Co and Pd in the electronic regulation of PtCoMoPdRh HEAs also discuss by XPS spectra. Comparative experiments and DFT calculations reveal that the multi-active sites and strain effect are contribute to the decrease water dissociation energy barriers and in favor of H adsorption, and thus accelerating the dynamics in both Volmer step and Tafel step during the alkaline HER process. This work not only provides a straightforward synthesis method for rational design Pt-based HEA nanomaterials, but also provide a fundamental theoretical study of HEA such as synergistic interaction and strain effect.
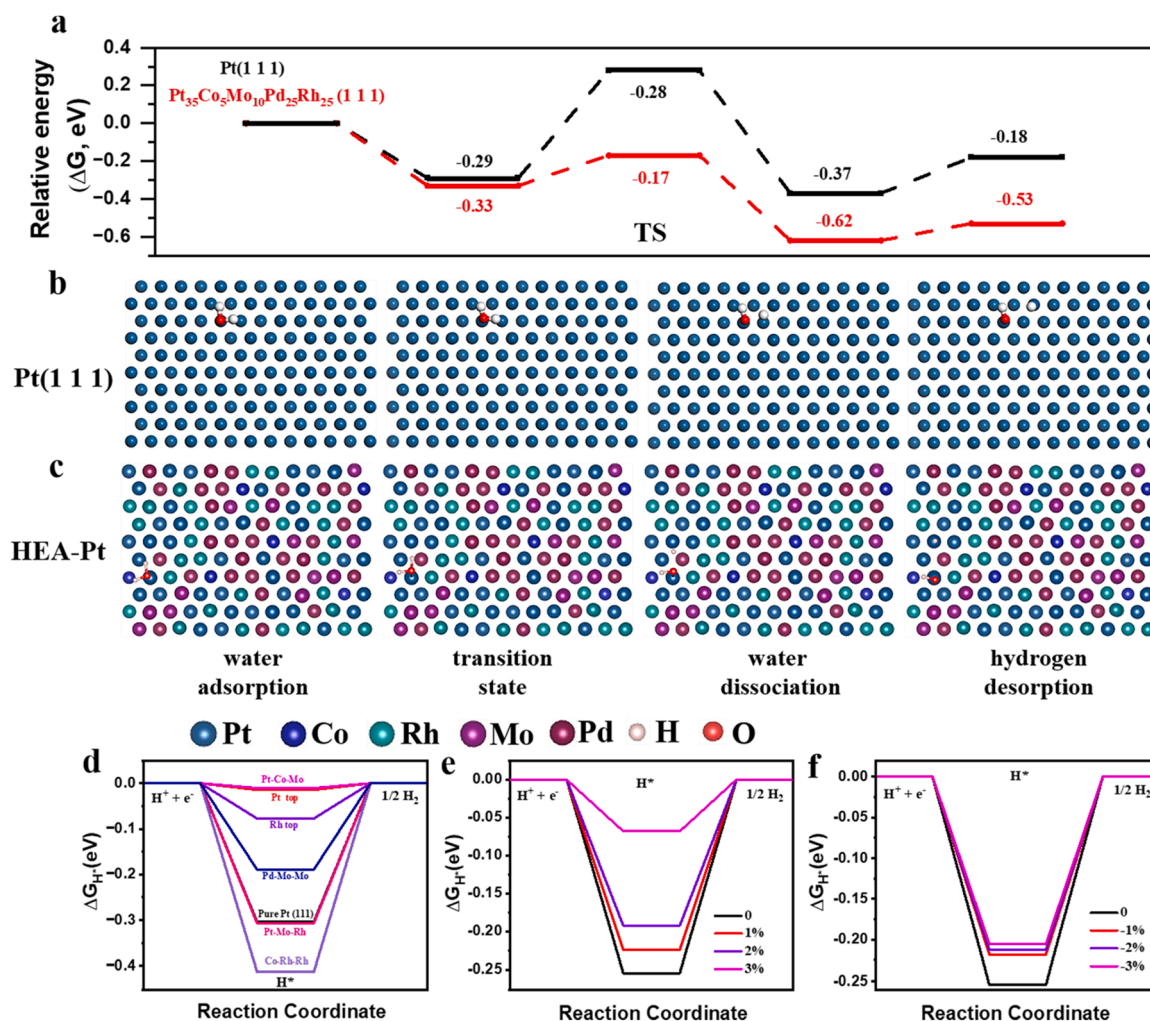
Fig. 4. Theoretical calculation of HER energy diagrams over pure Pt (1 1 1) and $Pt_{35}Co_5Mo_{10}Pd_{25}Rh_{25}$ (1 1 1). (a) Gibbs free energy diagram for alkaline HER on Pt (1 1 1) and $Pt_{35}Co_5Mo_{10}Pd_{25}Rh_{25}$ (1 1 1). (b) Binding configurations for pure Pt (1 1 1). (c) Binding configurations for pure $Pt_{35}Co_5Mo_{10}Pd_{25}Rh_{25}$ (1 1 1). (d) ΔG_{H^*} on various catalytic sites at $Pt_{35}Co_5Mo_{10}Pd_{25}Rh_{25}$ (1 1 1). Calculated free energy diagrams for hydrogen evolution of different lattice strain-optimized Pt16 of $Pt_{35}Co_5Mo_{10}Pd_{25}Rh_{25}$ (1 1 1), where the change in free energy caused by lattice is display in (e) compressive (from 0% to 3%) and (f) tensile (from −3% to 0).

CRediT authorship contribution statement

Min Wei (First Author): Conceptualization, Methodology, Investigation, Formal Analysis, Writing - Original Draft;**Yuyan Sun:** Data Curation , Investigation;**Fei Ai:** Data Curation , Investigation;**Shibo Xi:** Resources, Data Curation , **Junyu Zhang:** Investigation;**Jike Wang:** Conceptualization, Funding Acquisition, Software, Resources, Supervision, Writing - Review & Editing.

Declaration of Competing Interest

The authors declare that they have no known competing financial interests or personal relationships that could have appeared to influence the work reported in this paper.

Data availability

Data will be made available on request.

Acknowledgments

Appendix A. Supporting information

Supplementary data associated with this article can be found in the online version at doi:10.1016/j.apcatb.2023.122814.

References

[1] H.A. Gasteiger, N.M. Markovic, Chemistry. Just a dream–or future reality? Science 324 (2009) 48–49.
[2] N. Energy, Hydrogen on the rise, Nat. Energy 1 (2016) 1.
[3] Nicola Armaroli, Vincenzo Balzani, The future of energy supply: challenges and opportunities, Angew. Chem. Int. Ed. 46 (1–2) (2007) 52–66.
[4] I. Roger, M.A. Shipman, M.D. Symes, Earth-abundant catalysts for electrochemical and photoelectrochemical water splitting, Nat. Rev. Chem. 1 (2017) 0003.
[5] Q. Xu, L. Zhang, J. Zhang, J. Wang, Y. Hu, H. Jiang, C. Li, Anion exchange membrane water electrolyzer: electrode design, lab-scaled testing system and performance evaluation, EnergyChem 4 (2022).
[6] J. Wang, J. Zhang, Y. Hu, H. Jiang, C. Li, Activating multisite high-entropy alloy nanocrystals via enriching M-pyridinic N-C bonds for superior electrocatalytic hydrogen evolution, Sci. Bull. 67 (2022) 1890–1897.
[7] J. McHugh, D. Patrick, Stergiou Athanasios, D Mark Symes, Decoupled electrochemical water splitting: from fundamentals to applications, Adv. Energy Mater. 10 (2020) 2002453.
[8] J.E. Lee, K.J. Jeon, P.L. Show, I.H. lee, S.C. Jung, Y.J. Choi, G.H. Rhee, K.A. Lin, Y. K. Park, , Mini review on H_2 production from electrochemical water splitting according to special nanostructured morphology of electrocatalysts, Fuel 308 (2022), 122048.

[9] B. Ruqia, S.I. Choi, Pt and Pt–Ni (OH)$_2$ electrodes for the hydrogen evolution reaction in alkaline electrolytes and their nanoscaled electrocatalysts, ChemSusChem 11 (2018) 2643–2653.

[10] D. Kobayashi, H. Kobayashi, D. Wu, S. Okazoe, K. Kusada, T. Yamamoto, T. Toriyama, S. Matsumua, S. Kawaguchi, Y. Kubota, S.M. Aspera, H. Nakanishi, S. Arai, H. Kitagawa, Significant enhancement of hydrogen evolution reaction activity by negatively charged Pt through light doping of W, J. Am. Chem. Soc. 142 (2020) 17250–17254.

[11] P. Shi, R. Li, Y. Li, Y. Wen, Y. Zhong, W. Ren, Z. Shen, T. Zheng, J. Peng, X. Liang, P. Hu, N. Min, Y. Zhan, Y. Ren, P.K. Liaw, D. Raabe, Y.-D. Wang, Hierarchical crack buffering triples ductility in eutectic herringbone high-entropy alloys, Science 373 (2021) 912–918.

[12] Y. Zheng, Y. Yi, M. Fan, H. Liu, X. Li, R. Zhang, M. Li, Z.-A. Qiao, A high-entropy metal oxide as chemical anchor of polysulfide for lithium-sulfur batteries, Energy Storage Mater. 23 (2019) 678–683.

[13] D. Feng, Y. Dong, L. Zhang, X. Ge, W. Zhang, S. Dai, Z.A. Qiao, Holey lamellar high-entropy oxide as an ultra-high-activity heterogeneous catalyst for solvent-free aerobic oxidation of benzyl, Alcohol, Angew. Chem. Int. Ed. Engl. 59 (2020) 19503–19509.

[14] T.A. Batchelor, J.K. Pedersen, S.H. Winther, I.E. Castelli, K.W. Jacobsen, J. Rossmeisl, High-entropy alloys as a discovery platform for electrocatalysis, Joule 3 (2019) 834–845.

[15] G.M. Tomboc, T. Kwon, J. Joo, K. Lee, High entropy alloy electrocatalysts: a critical assessment of fabrication and performance, J. Mater. Chem. A 8 (2020) 14844–14862.

[16] T. Löffler, A. Ludwig, J. Rossmeisl, W. Schuhmann, What makes high-entropy alloys exceptional electrocatalysts? Angew. Chem. Int. Ed. 60 (2021) 26894–26903.

[17] H. Li, Y. Han, H. Zhao, W. Qi, D. Zhang, Y. Yu, W. Cai, S. Li, J. Lai, B. Huang, L. Wang, Fast site-to-site electron transfer of high-entropy alloy nanocatalyst driving redox electrocatalysis, Nat. Commun. 11 (2020) 5437.

[18] D. Zhang, H. Zhao, X. Wu, Y. Deng, Z. Wang, Y. Han, H. Li, Y. Shi, X. Chen, S. Li, J. Lai, B. Huang, L. Wang, Multi-site electrocatalysts boost pH-universal nitrogen reduction by high-entropy alloys, Adv. Funct. Mater. 31 (2020), 2006939.

[19] G. Feng, F. Ning, J. Song, H. Shang, K. Zhang, Z. Ding, P. Gao, W. Chu, D. Xia, Sub-2 nm ultrasmall high-entropy alloy nanoparticles for extremely superior electrocatalytic hydrogen evolution, J. Am. Chem. Soc. 143 (2021) 17117–17127.

[20] M.P. Browne, Z. Sofer, M. Pumera, Layered and two dimensional metal oxides for electrochemical energy conversion, Energy Environ. Sci. 12 (2019) 41–58.

[21] M. Luo, Z. Zhao, Y. Zhang, Y. Sun, Y. Xing, F. Lv, Y. Yang, X. Zhang, S. Hwang, Y. Qin, J.Y. Ma, F. Lin, D. Su, G. Lu, S. Guo, PdMo bimetallene for oxygen reduction catalysis, Nature 574 (2019) 81–85.

[22] W. Chen, W. Gao, P. Tu, T. Robert, Y. Ma, H. Shan, X. Gu, W. Shang, P. Tao, C. Song, T. Deng, H. Zhu, X. Pan, H. Yang, J. Wu, Neighboring Pt atom sites in an ultrathin FePt nanosheet for the efficient and highly CO-tolerant oxygen reduction reaction, Nano Lett. 18 (2018) 5905–5912.

[23] T. Kwon, M. Jun, H.Y. Kim, A. Oh, J. Park, H. Baik, S.H. Joo, K. Lee, Vertex-reinforced PtCuCo ternary nanoframes as efficient and stable electrocatalysts for the oxygen reduction reaction and the methanol oxidation reaction, Adv. Funct. Mater. 28 (2018), 1706440.

[24] E.P. George, D. Raabe, R.O. Ritchie, High-entropy alloys, Nat. Rev. Mater. 4 (2019) 515–534.

[25] S. Maiti, K. Maiti, M.T. Curnan, K. Kim, K.J. Noh, J.W. Han, Engineering electrocatalyst nanosurfaces to enrich the activity by inducing lattice strain, Energy Environ. Sci. 14 (2021) 3717–3756.

[26] D.J. Weber, C. Dosche, M. Oezaslan, Tuning of Pt–Co nanoparticle motifs for enhancing the HOR performance in alkaline media, J. Mater. Chem. A 9 (2021) 15415–15431.

[27] Y. Dai, K. Sun, Y. Li, Mo@Pt core–shell nanoparticles as an efficient electrocatalyst for oxygen reduction reaction, J. Electroanal. Chem. 757 (2015) 94–99.

[28] Q.T. Trinh, J. Yang, J.Y. Lee, Computational and experimental study of the Volcano behavior of the oxygen reduction activity of PdM@ PdPt/C (M= Pt, Ni, Co, Fe, and Cr) core–shell electrocatalysts, J. Catal. 291 (2012) 26–35.

[29] Y. Zhu, L. Bu, Q. Shao, X. Huang, Subnanometer PtRh nanowire with alleviated poisoning effect and enhanced C–C bond cleavage for ethanol oxidation electrocatalysis, ACS Catal. 9 (2019) 6607–6612.

[30] M.H.M.T. Assumpção, R.M. Piasentin, P. Hammer, R.F. De Souza, B. Souza, G. S. Buzzo, M.C. Santos, E.V. Spinace, A.O. Neto, J.C.M. Silva, , Oxidation of ammonia using PtRh/C electrocatalysts: fuel cell and electrochemical evaluation, Appl. Catal. B 174 (2015) 136–144.

[31] J. Hao, Z. Zhuang, K. Cao, G. Gao, C. Wang, F. Lai, S. Lu, P. Ma, W. Dong, T. Liu, M. Du, H. Zhu, Unraveling the electronegativity-dominated intermediate adsorption on high-entropy alloy electrocatalysts, Nat. Commun. 13 (1) (2022) 2662.

[32] S. Dai, J.P. Chou, K.W. Wang, Y.Y. Hsu, A. Hu, X. Pan, T.Y. Chen, Platinum-trimer decorated cobalt-palladium core–shell nanocatalyst with promising performance for oxygen reduction reaction, Nat. Commun. 10 (2019) 440.

[33] S. Fang, X. Zhu, X. Liu, J. Gu, W. Liu, D. Wang, W. Zhang, Y. Lin, J. Lu, S. Wei, Y. Li, T. Yao, Uncovering near-free platinum single-atom dynamics during electrochemical hydrogen evolution reaction, Nat. Commun. 11 (2020) 1029.

[34] E.K. Hli, R. Baudoing-Savois, B. Moraweck, A.J. Renouprez, X-ray absorption edges in platinum-based alloys. 2. Influence of ordering and of the nature of the second metal, J. Phys. Chem. 100 (1996) 3102–3107.

[35] C.C. McCrory, S. Jung, I.M. Ferrer, S.M. Chatman, J.C. Peters, T.F. Jaramillo, Benchmarking hydrogen evolving reaction and oxygen evolving reaction electrocatalysts for solar water splitting devices, J. Am. Chem. Soc. 137 (2015) 4347–4357.

[36] C. Panda, P.W. Menezes, S. Yao, J. Schmidt, C. Walter, J.N. Hausmann, M. Driess, Boosting electrocatalytic hydrogen evolution activity with a NiPt$_3$@NiS heteronanostructure evolved from a molecular nickel-platinum precursor, J. Am. Chem. Soc. 141 (2019) 13306–13310.

[37] X. Chia, N.A.A. Sutrisnoh, M. Pumera, Tunable Pt-MoSx hybrid catalysts for hydrogen evolution, ACS Appl. Mater. Interfaces 10 (2018) 8702–8711.

[38] J.D. Benck, T.R. Hellstern, J. Kibsgaard, P. Chakthranont, T.F. Jaramillo, Catalyzing the hydrogen evolution reaction (HER) with molybdenum sulfide nanomaterials, ACS Catal. 4 (2014) 3957–3971.

[39] S. Jing, J. Lu, G. Yu, S. Yin, L. Luo, Z. Zhang, Y. Ma, W. Chen, P.K. Shen, Carbon-encapsulated WOx hybrids as efficient catalysts for hydrogen evolution, Adv. Mater. 30 (2018), e1705979.

[40] H. Vrubel, X. Hu, Molybdenum boride and carbide catalyze hydrogen evolution in both acidic and basic solutions, Angew. Chem. Int. Ed. 51 (2012) 12703–12706.

[41] S. Wang, B. Xu, W. Huo, H. Feng, X. Zhou, F. Fang, Z. Xie, J.K. Shang, J. Jiang, Efficient FeCoNiCuPd thin-film electrocatalyst for alkaline oxygen and hydrogen evolution reactions, Appl. Catal. B 313 (2022) 121472.

[42] S. Nellaiappan, N.K. Katiyar, R. Kumar, A. Parui, K.D. Malviya, K.G. Pradeep, A. K. Singh, S. Sharma, C.S. Tiwary, K. Biswas, High-entropy alloys as catalysts for the CO$_2$ and CO reduction reactions: experimental realization, ACS Catal. 10 (2020) 3658–3663.

[43] W.T. Cahyanto, S. Zulaehah, W. Widanarto, F. Abdullatif, M. Effendi, H. Kasai, Theoretical study of an almost barrier-free water dissociation on a platinum (111) surface alloyed with ruthenium and molybdenum, ACS Omega 6 (2021) 10770–10775.

[44] N. Yao, P. Li, Z. Zhou, Y. Zhao, G. Cheng, S. Chen, W. Luo, Synergistically tuning water and hydrogen binding abilities over Co$_4$N by Cr doping for exceptional alkaline hydrogen evolution electrocatalysis, Adv. Energy Mater. 9 (2019).

[45] J.K. Norskov, T. Bligaard, J. Rossmeisl, C.H. Christensen, Towards the computational design of solid catalysts, Nat. Chem. 1 (2009) 37–46.

[46] H. Huang, H. Jia, Z. Liu, P. Gao, J. Zhao, Z. Luo, J. Yang, J. Zeng, Understanding of strain effects in the electrochemical reduction of CO$_2$: using Pd nanostructures as an ideal platform, Angew. Chem. Int. Ed. Engl. 56 (2017) 3594–3598.